

The Luminous and Double-Peaked Type Ic Supernova 2019stc: Evidence for Multiple Energy Sources

SEBASTIAN GOMEZ,¹ EDO BERGER,¹ GRIFFIN HOSSEINZADEH,¹ PETER K. BLANCHARD,² MATT NICHOLL,³ AND
V. ASHLEY VILLAR^{4,*}

¹Center for Astrophysics | Harvard & Smithsonian, 60 Garden Street, Cambridge, MA 02138, USA

²Center for Interdisciplinary Exploration and Research in Astrophysics and Department of Physics and Astronomy,
Northwestern University, 1800 Sherman Ave, Evanston, IL 60201, USA

³Birmingham Institute for Gravitational Wave Astronomy and School of Physics and Astronomy, University of Birmingham,
Birmingham B15 2TT, UK

⁴Department of Astronomy, Columbia University, New York, NY 10027-6601, USA

ABSTRACT

We present optical photometry and spectroscopy of SN 2019stc (=ZTF19acbonaa), an unusual Type Ic supernova (SN Ic) at a redshift of $z = 0.117$. SN 2019stc exhibits a broad double-peaked light curve, with the first peak having an absolute magnitude of $M_r = -20.0$ mag, and the second peak, about 80 rest-frame days later, $M_r = -19.2$ mag. The total radiated energy is large, $E_{\text{rad}} \approx 2.5 \times 10^{50}$ erg. Despite its large luminosity, approaching those of Type I superluminous supernovae (SLSNe), SN 2019stc exhibits a typical SN Ic spectrum, bridging the gap between SLSNe and SNe Ic. The spectra indicate the presence of Fe-peak elements, but modeling of the first light curve peak with radioactive heating alone leads to an unusually high nickel mass fraction of $f_{\text{Ni}} \approx 0.31$ ($M_{\text{Ni}} \approx 3.2 M_{\odot}$). Instead, if we model the first peak with a combined magnetar spin-down and radioactive heating model we find a better match with $M_{\text{ej}} \approx 4 M_{\odot}$, a magnetar spin period of $P_{\text{spin}} \approx 7.2$ ms and magnetic field of $B \approx 10^{14}$ G, and $f_{\text{Ni}} \lesssim 0.2$ (consistent with SNe Ic). The prominent second peak cannot be naturally accommodated with radioactive heating or magnetar spin-down, but instead can be explained as circumstellar interaction with $\approx 0.7 M_{\odot}$ of hydrogen-free material located ≈ 400 AU from the progenitor. Accounting for the ejecta mass, CSM shell mass, and remnant neutron star mass, we infer a CO core mass prior to explosion of $\approx 6.5 M_{\odot}$. The host galaxy has a metallicity of $\approx 0.26 Z_{\odot}$, low for SNe Ic but consistent with SLSNe. Overall, we find that SN 2019stc is a transition object between normal SNe Ic and SLSNe.

Keywords: supernova: general – supernova: individual (SN 2019stc)

1. INTRODUCTION

Stars more massive than $\approx 8 M_{\odot}$ are expected to end their lives in core collapse supernova (CCSN) explosions. Among these, Type Ic SNe (SNe Ic) are the explosions of stars that have lost their hydrogen and helium envelopes. SNe Ic have typical peak magnitudes of $M_r = -17.7 \pm 0.8$ mag (e.g., Filippenko 1997; Lyman et al. 2016; Prentice et al. 2016; Fremling et al. 2018; Prentice et al. 2019; Barbarino et al. 2020), while the subset of broad-lined SNe Ic (SNe Ic-BL) can reach peak magnitudes of up to ≈ -19.4 mag (Taddia et al. 2019b). It is

well established that SNe Ic are powered by the radioactive decay of ^{56}Ni synthesized in the explosion, with typical nickel masses of $M_{\text{Ni}} \approx 0.05 - 0.6 M_{\odot}$, or nickel fractions of $f_{\text{Ni}} \approx 0.05 - 0.3$ (Drout et al. 2011; Taddia et al. 2019b; Barbarino et al. 2020). In terms of their environments, SNe Ic tend to occur in galaxies with relatively high metallicities of $12 + \log(\text{O}/\text{H}) = 8.8 \pm 0.2$ (Modjaz et al. 2020).

Type I superluminous supernovae (SLSNe) on the other hand are a much more rare type of CCSNe. SLSNe also represent the explosions of stripped stars, but they be up to 100 times more luminous than SNe Ic, with peak magnitudes of $M_r \approx -20.0$ to -23 mag (e.g., Chomiuk et al. 2011; Quimby et al. 2011; Lunnan et al. 2013; Gal-Yam 2019; Gomez et al. 2020a). Their early time spectra tend to be blue and characterised by oxygen features near $\sim 4000 \text{ \AA}$ (e.g, Gal-Yam 2012; Nicholl

Corresponding author: Sebastian Gomez
sgomez@cfa.harvard.edu

* Simons Junior Fellow

et al. 2017a), but their late time spectra are closer to those of SNe Ic at earlier phases (e.g., Quimby et al. 2018; Nicholl et al. 2019). The primary energy source of SLSNe appears to be the spin-down energy of a newly formed millisecond magnetar, with typical spin periods of $P_{\text{spin}} \approx 1.2 - 4$ ms and magnetic fields of $B \approx 0.2 - 1.8 \times 10^{14}$ G (Nicholl et al. 2017b). More recently, the ejecta masses of SLSNe have been shown to extend to $\approx 40 M_{\odot}$, much higher than for SNe Ic (Blanchard et al. 2020). SLSNe are known to be over-represented in low metallicity galaxies, which have typical metallicities of $12 + \log(\text{O}/\text{H}) = 8.4 \pm 0.3$ (Lunnan et al. 2014).

CCSNe with luminosities intermediate to SNe Ic and SLSNe, as well as their detailed properties and relation to the other classes, remains mostly unexplored. Only a handful of events with peak magnitudes in the $M_r = -19$ to -20.0 range are known (SN 2018gep Ho et al. 2019, SN 2018bsz Anderson et al. 2018, SN 2011kl Greiner et al. 2015, SN 2012aa Roy et al. 2016, and DES14C1rhg and DES15C3hav Angus et al. 2019). Such intermediate events may potentially be powered by radioactivity and/or a magnetar engine, and can therefore shed light on the relation between the energy sources and progenitors of the various types of stripped CCSNe.

Here, we present detailed optical observations of an intriguing event intermediate to SNe Ic and SLSNe. Originally classified as a SLSN-I by Yan et al. (2020 a), SN 2019stc exhibits a spectrum typical of SNe Ic at all phases of its evolution. Its light curve is peculiar in several ways: it is unusually luminous ($M_r \approx -20$ mag), unusually broad (rise time of 40 rest-frame days), exhibits a prominent second peak ($M_r \approx -19.2$ mag) about 80 rest-frame days after the first peak, and radiated $\approx 2.5 \times 10^{50}$ erg. From analytical models we find that the first peak is predominantly powered by a magnetar engine, but with possible contribution from radioactive heating at a level typical of SNe Ic (thus explaining the spectral appearance). The second peak is most likely explained as delayed circumstellar interaction with a shell ejected prior to the SN explosion.

The paper is structured as follows: in §2 we present our classification and follow-up observations of SN 2019stc, as well as publicly available data. We describe the multi-color and bolometric light curves in §3, and the optical spectra in §4. In §5 we present a range of analytical models of the light curve, and in §6 we describe the host galaxy properties. In §7 we discuss possible interpretations of SN 2019stc and present our conclusions. Throughout the paper we assume a flat Λ CDM cosmology with $H_0 = 69.3 \text{ km s}^{-1} \text{ Mpc}^{-1}$, $\Omega_m = 0.286$, and $\Omega_{\Lambda} = 0.712$ (Hinshaw et al. 2013).

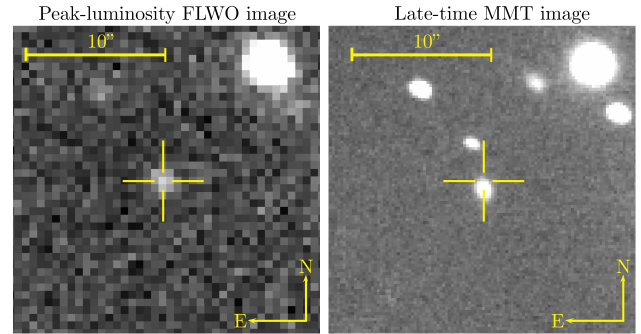


Figure 1. Optical *i*-band images of the field of SN 2019stc. *Left:* Our first FLWO image taken at MJD = 58818 (phase = 22 days). *Right:* Our last MMT image taken at MJD = 59174 (phase = 340 days) that shows a contribution from only the host galaxy. We see the SN is located on the outskirts of the host galaxy.

2. OBSERVATIONS

2.1. Discovery

SN 2019stc was first detected as a transient by the Zwicky Transient Facility (ZTF; Bellm et al. 2019) on 2019 September 30 at R.A.= $06^{\text{h}}54^{\text{m}}23^{\text{s}}.10$, decl.= $+17^{\circ}29'31''.35$ (J2000) with a magnitude of $m_r = 19.95$ mag and designated ZTF19acbonaa. We triggered follow-up spectroscopic observations of the transient as part of our *Finding Luminous and Exotic Extragalactic Transients* (FLEET) observational program designed to find SLSNe (Gomez et al. 2020a).

2.2. Optical Photometry

We obtained optical images of SN 2019stc in the *griz* filters with three different telescopes: KeplerCam on the 1.2-m telescope at Fred Lawrence Whipple Observatory (FLWO); the Low Dispersion Survey Spectrograph (LDSS3c; Stevenson et al. 2016) on the Magellan Clay 6.5-m telescope at Las Campanas Observatory, and Binospec (Fabricant et al. 2019) on the MMT 6.5-m telescope. We reduced the images using standard IRAF¹ routines, and performed photometry with the *daophot* package.

Instrumental magnitudes were measured by modeling the point-spread function (PSF) of each image using field stars and subtracting the model PSF from the target (Figure 1). To separate the flux of SN 2019stc from that of its host galaxy we perform image subtraction on each image with HOTPANTS (Becker 2015), using archival

¹ IRAF is written and supported by the National Optical Astronomy Observatories, operated by the Association of Universities for Research in Astronomy, Inc. under cooperative agreement with the National Science Foundation.

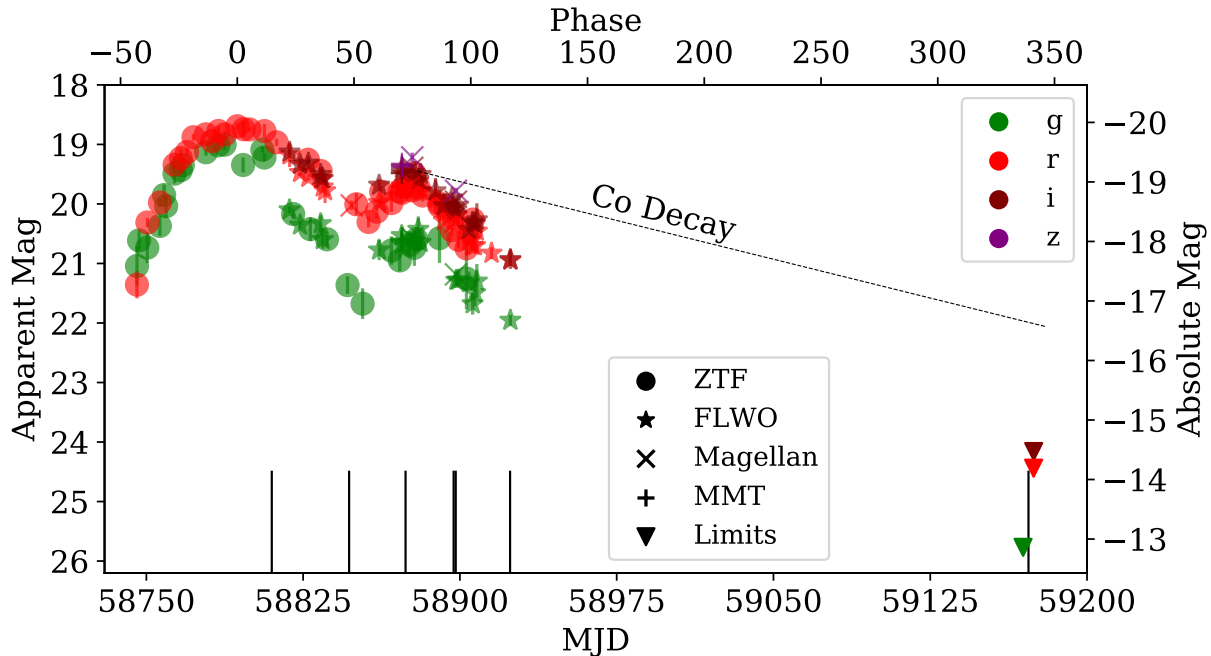


Figure 2. Optical light curves of SN 2019stc in the *griz* bands. Magnitudes are in the AB system and not corrected for Galactic extinction. Absolute magnitudes have an additional cosmological K-correction applied. The vertical lines mark the epochs of spectroscopy. The final upper limits are 3σ non-detections from deep MMT+Binospic images.

PS1/ 3π images as reference templates. We estimate individual zero-points of each image by measuring the magnitudes of field stars and comparing to photometric AB magnitudes from the PS1/ 3π catalog (Chambers & Pan-STARRS Team 2018). The uncertainties reported here are the combination of the photometric uncertainty and the uncertainty in the zero-point determination.

We include additional photometry from ZTF images. In order to recover any detections of SN 2019stc not reported by the automated ZTF pipeline we downloaded the original ZTF images from the NASA/IPAC Infrared Science Archive². We performed photometry on these images in the same way as the FLWO images described above. All the photometry used for this work is provided in machine readable format in the online version of this paper and on the Open Supernova Catalog³ (Guillochon et al. 2017). All data are provided before correcting for Galactic extinction and calibrated to PS1 AB magnitudes.

The full multi-color light curves of SN 2019stc are shown in Figure 2, where we define phase 0 to be the date of the brightest *r*-band magnitude, MJD = 58793.5. We use this reference date throughout the paper, with all days quoted in the rest frame unless otherwise noted.

Absolute magnitudes have an additional cosmological K-correction applied of $+2.5 \log(1+z)$. All of the photometry is corrected for Galactic extinction using $A_V = 3.1$ and $E(B-V) = 0.084$ mag, according to the dust maps from Schlafly & Finkbeiner (2011). We use the Barbary (2016) implementation of the Cardelli et al. (1989) extinction law to correct the photometry. Based on the expectation from case B recombination, we determine that host galaxy extinction corrections are not necessary (described further in §6).

Our final epoch of imaging, in *gri*, was obtained on 2019 November 11 with Binospic on MMT. We do not detect SN 2019stc down to a magnitude of $r > 24.2$, $g > 25.4$, and $i > 24.0$. These are 3σ upper limits obtained from forced photometry at the location of SN 2019stc on difference images with subtracted PS1/ 3π reference templates.

2.3. Optical Spectroscopy

We obtained seven epochs of low-resolution optical spectroscopy covering phases from 15 to 340 days. We used the LDSS3c Spectrograph (Stevenson et al. 2016) and Inamori-Magellan Areal Camera and Spectrograph (IMACS; Dressler et al. 2011) on the Magellan 6.5-m telescopes and the Blue Channel (Schmidt et al. 1989) and Binospic (Fabricant et al. 2003) spectrographs on the MMT 6.5-m telescope. All the spectra were obtained with the slit oriented along the parallactic angle.

² <https://irsa.ipac.caltech.edu/Missions/ztf.html>

³ <https://sne.space/>

Table 1. Log of Optical Spectroscopic Observations

UT Date	MJD	Phase	Exp. Time	Airmass	Wavelength Range	Instrument	Grating
		(d)	(s)		(Å)		(lines/mm)
2019 Nov 23	58810.0	+15	1200	1.2	3820–9210	Binospec	270
2019 Dec 30	58847.0	+48	2400	1.6	4210–8890	IMACS	300
2020 Jan 26	58874.0	+72	2700	1.2	3820–9210	Binospec	270
2020 Feb 18	58897.0	+93	1800	1.1	3320–8540	Blue Channel	300
2020 Feb 19	58898.0	+94	1500	1.5	4000–9270	LDSS3c	400
2020 Mar 16	58924.0	+117	2400	1.0	3820–9210	Binospec	270
2020 Nov 19	59172.0	+339	4800	1.6	4800–9790	LDSS3c	400

NOTE—All observations were taken with a 1'' slit width.

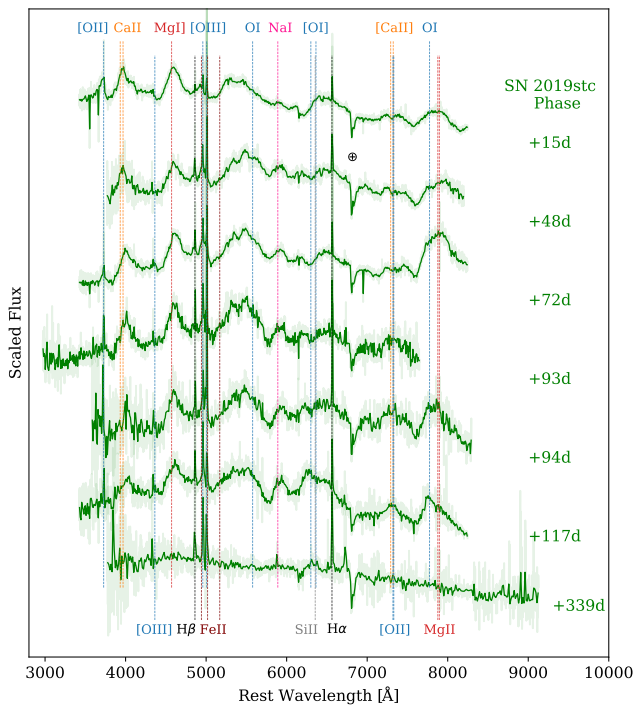


Figure 3. Optical spectra of SN 2019stc, corrected for Galactic extinction and shifted to the rest-frame of SN 2019stc using $z = 0.117$. We binned the spectra for clarity and show the unbinned spectra as shaded regions. Relevant spectral lines are marked. The last spectrum at a phase of 339 days is dominated by host galaxy emission.

Details of the spectroscopic observations are provided in Table 1.

We reduced the spectra using standard IRAF¹ routines using the `twodspec` package. The spectra were bias-subtracted and flat-fielded, the sky background was modeled and subtracted from each image, and the one-dimensional spectra were optimally extracted, weighing by the inverse variance of the data. A wavelength cali-

bration was applied using an arc lamp spectrum taken near the time of each science image. Relative flux calibration was applied to each spectrum using a standard star taken close to the time of observation. The spectra were then calibrated to absolute flux using our *gri* photometry as a reference, applying a normalization constant to each spectrum to match the expected flux from the photometry using the PYPHOT Python package. Lastly, the spectra were corrected for Galactic extinction using $E(B - V) = 0.084$ and transformed to the rest frame of SN 2019stc using $z = 0.117$. All the spectroscopy collected for this work is made available on WISeREP⁴ (Yaron & Gal-Yam 2012) and the Open Supernova Catalog³ (Guillochon et al. 2017), after flux calibrating but before correcting for Galactic extinction and redshift. The spectra are shown in Figure 3.

3. LIGHT CURVES

The light curve of SN 2019stc exhibits a peculiar and pronounced double-peaked structure, clearly seen in all available filters (Figure 2). The first peak reaches $M_r = -20.0$ at 58793.5 MJD, with a rise time of ~ 40 days. Subsequently, the light curve declines at a rate of 0.033 ± 0.004 mag day⁻¹. ~ 53 rest days after the first peak, the light curve begins to re-brighten and produces a second peak with $M_r = -19.2$ (at 58882 MJD), 79 rest-frame days after the first peak. After the second peak, the light curve declines at a rate of 0.036 ± 0.003 mag day⁻¹. This decline rate is much too fast to be consistent with Co decay’s rate of ≈ 0.01 mag day⁻¹, suggesting that the second peak is not due to radioactive decay.

In Figure 4 we compare the light curve of SN 2019stc to those of both normal and long-lived stripped SNe, with a specific focus on luminous events and other events

⁴ <https://wiserep.weizmann.ac.il/>

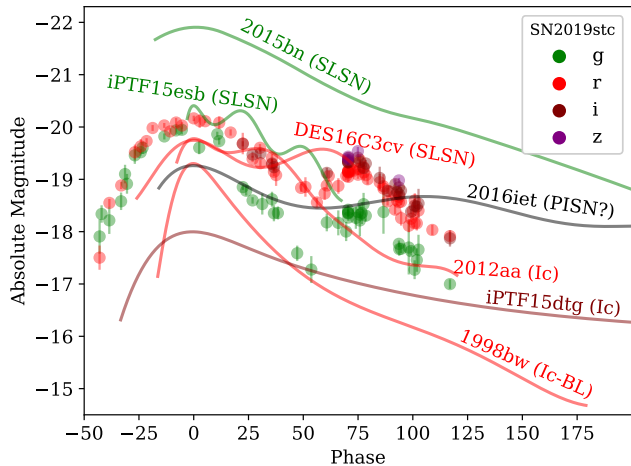


Figure 4. Light curve of SN 2019stc compared to several other luminous and/or double-peaked hydrogen-poor SNe: SN 2015bn (Nicholl et al. 2016a,b, 2018), iPTF15esb (Yan et al. 2017), SN 2016iet (Gomez et al. 2019), SN 2012aa (Roy et al. 2016), iPTF15dtg (Taddia et al. 2019a), DES16C3cv Angus et al. (2019), and SN 1998bw (Galama et al. 1998). The comparison light curves have been smoothed for clarity using a 1-D spline and shifted in phase to match the first peak of SN 2019stc. For SN 2016iet we smooth a combination of G, C, and *i* bands given its sparse multi-band coverage at early times. None of the comparison SNe show a double-peak structure as pronounced as SN 2019stc.

that have showed a double peaked structure. The first peak of SN 2019stc is more luminous and broader than even the broad-lined Type Ic SN 1998bw (Galama et al. 1998), much less bright than the archetype SLSN 2015bn (Nicholl et al. 2016a), and significantly brighter than normal SNe Ic (e.g., iPTF15dtg Taddia et al. 2019a). Other events such as iPTF15esb (Yan et al. 2017) or SN 2012aa (Roy et al. 2016) exhibit undulations in their light curves, but all with a much lower amplitude and on much shorter timescales than SN 2019stc. Spectroscopically, iPTF15esb is a SLSN that showed late-time H α emission, while SN 2012aa has a spectral sequence that shares similarities that place it between the SLSNe and SNe Ic population. A similar light curve structure was also seen in the SLSN DES16C3cv, where the two peaks are separated by ≈ 60 days (Angus et al. 2019). Additionally, we show SN 2016iet, a hydrogen and helium free pulsational pair-instability SN (PPISN) candidate in which the two peaks were separated by 100 days and are comparable in luminosity to SN 2019stc (Gomez et al. 2019). However, we note that the peaks in DES16C3cv and SN 2016iet are less pronounced than in SN 2019stc. Therefore, we conclude that SN 2019stc is unique among the hydrogen/helium-poor SN class in terms of its light curve properties.

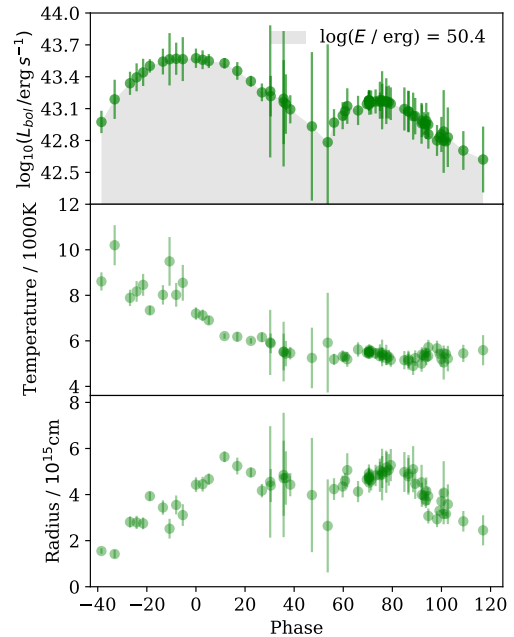


Figure 5. Time evolution of the bolometric light curve (*Top*), blackbody temperature (*Middle*), and photospheric radius (*Bottom*) of SN 2019stc. The shaded gray region indicates the area over which we determine the total radiated energy, which we find to be $E_{\text{rad}} \approx 2.5 \times 10^{50}$ erg. The increase in photospheric radius during the second peak is possibly indicative of CSM interaction and the formation of a new photosphere in the interaction region.

We calculate the bolometric light curve of SN 2019stc, its photospheric radius, and temperature evolution by fitting the spectral energy distribution (SED) of each epoch with a blackbody function using the `Superbol` code (Nicholl 2018). We further extrapolate the blackbody SED to account for the missing coverage in the UV and NIR. The resulting bolometric light curve, photospheric radius, and temperature evolution are shown in Figure 5. The error bars represent the uncertainties in the measurement of luminosity, temperature, and radius; which are affected by a combination of the photometric error bars, the uncertainty in the light curve interpolation, and the blackbody fits. The error bars for the epochs between ~ 30 to ~ 50 days are particularly affected due to the uncertainty in the interpolation when the light curve is turning over. To mitigate this issue and due to the fact we only have photometry in two bands during this epoch, we include one synthetic *i*-band data point to the `Superbol` interpolation at MJD = 58847.0, obtained from a convolution of the corresponding spectrum. The total integrated energy in the observed epochs between a phase of -38 and 117 days is

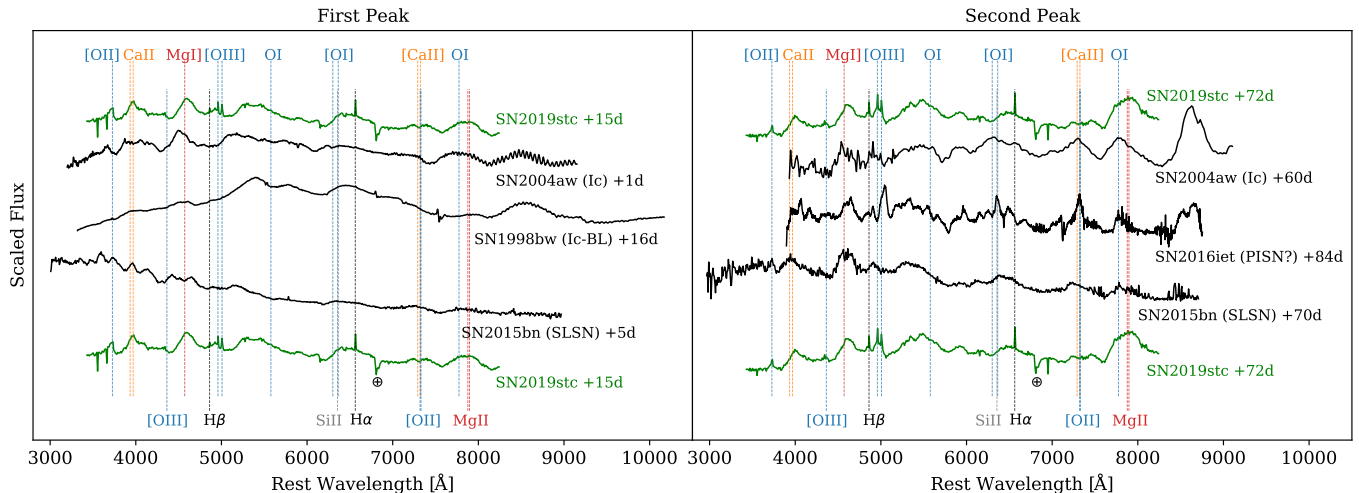


Figure 6. Spectra of SN 2019stc (green) during the first (*Left*) and second (*Right*) peaks, compared to other representative stripped envelope SNe (black): SN 1998bw (Patat et al. 2001), SN 2004aw (Modjaz et al. 2014), SN 2016iet (Gomez et al. 2019), and SN 2015bn (Nicholl et al. 2016a). The vertical lines mark the locations of dominant spectral features and \oplus marks telluric features. The SN 2019stc spectra has been binned for clarity. We find that SN 2019stc most closely matches the normal SN Ic SN 2004aw, and is clearly distinct from the other comparison SNe.

$E_{\text{rad}} \approx 2.5 \times 10^{50}$ erg. This is over an order of magnitude larger than for normal SNe Ic (Prentice et al. 2016).

The blackbody temperature during the first peak is about 8500 K, which then steadily decreases to about 5500 K by the time the second peak begins and stays at that value throughout the remainder of the light curve. The photospheric radius initially increases through the first peak to a maximum value of about 5.5×10^{15} cm, then recedes to about 4×10^{15} cm, increases again through the second peak (to about 5.5×10^{15} cm), and finally declines steadily following the second peak. We note that the increase in photospheric radius during the second peak could be a signature of CSM interaction, as a new photosphere would form in the interaction region.

4. SPECTRAL FEATURES

Our optical spectra of SN 2019stc span 15 to 339 days after peak (Figure 3). The spectra are typical of a normal SN Ic, with no evidence of hydrogen or helium lines and a downturn in the flux blueward of about 5000 Å. This is different from most SLSNe, which exhibit a significantly bluer continuum (e.g., Howell et al. 2013; Nicholl et al. 2016a; Quimby et al. 2018), although some do show a similar downturn below ~ 5000 Å (e.g., SN 2017dwh; Blanchard et al. 2019). We do not see a dramatic evolution in the spectra from 15 days after peak to 72 days after peak, other than a redder color. The spectra are dominated by broad lines of Mg, Ca, Fe, and O. We fit the absorption component present in the O I $\lambda 7774$, Na I $\lambda 5890$, Mg I $\lambda 4571$, and Si II $\lambda 6355$ lines with a Gaussian profile and use the center of these to es-

timate the velocity of the ejecta. We obtain an average ejecta velocity by measuring the center of the absorption component of the O I $\lambda 7774$ lines in our spectra and obtain a value of 7800 ± 1900 km s $^{-1}$, roughly constant and comparable to the velocities of SNe Ic near peak (Taddia et al. 2019b).

In Figure 6 we compare the spectra of SN 2019stc during the first and second peaks to those of several stripped SNe: SN 1998bw (Ic-BL; Patat et al. 2001), SN 2004aw (Ic; Modjaz et al. 2014), SN 2016iet (PISN candidate; Gomez et al. 2019), and SN 2015bn (SLSN; Nicholl et al. 2016a). During the first peak the spectral features in SN 2019stc are significantly narrower than in the broad-lined SN 1998bw (which has $V \approx 30,000$ km s $^{-1}$), and slower than in the normal Ic SN 2004aw, which had a velocity of $V_{\text{ej}} \approx 11,100$ km s $^{-1}$ near peak (Taubenberger et al. 2006; Mazzali et al. 2017). The spectra of SN 2019stc are significantly redder at $\lesssim 5000$ Å than that of the SLSN 2015bn and lack the characteristic oxygen features near ~ 4000 Å found in SLSNe. During the second peak, SN 2019stc still closely resembles SN 2004aw, and is still redder than SN 2015bn. It also appears distinct from SN 2016iet, which partially resembles a SN Ic, but has a bluer continuum and narrower spectral features than SN 2019stc. We therefore conclude that spectroscopically SN 2019stc most closely matches a normal SN Ic during both the first and second peak.

5. LIGHT CURVE MODELING

Table 2. MOSFiT Parameter Definitions

Parameter	Definition
M_{ej}	Ejecta mass
M_{Ni}	Radioactive nickel mass
f_{Ni}	Nickel mass as a fraction of the ejecta mass
v_{ej}	Ejecta velocity
E_k	Ejecta kinetic energy
R_0	CSM inner radius
ρ_0	CSM density at R_0
M_{NS}	Neutron star mass
P_{spin}	Magnetar spin
B_{\perp}	Magnetar magnetic field strength
θ_{BP}	Angle of the dipole moment
t_{exp}	Explosion time relative to first data point
T_{min}	Photosphere temperature floor
λ_{cut}	Flux below this wavelength is suppressed
$n_{H,\text{host}}$	Column density in the host galaxy
$A_{V,\text{host}}$	Extinction in the host galaxy
κ	Optical opacity
κ_{γ}	Gamma-ray opacity
σ	Uncertainty required for $\chi_r^2 = 1$

We model the light curves of SN 2019stc using the Modular Open-Source Fitter for Transients (MOSFiT) Python package, a flexible code that uses a Markov chain Monte Carlo (MCMC) implementation to fit the light curves of transients using a variety of different power sources (Guillochon et al. 2018). We run each MCMC using an implementation of the emcee sampler (Foreman-Mackey et al. 2013). We test for convergence by ensuring that the models reach a potential scale reduction factor of < 1.2 (Gelman & Rubin 1992), which corresponds to about 35,000 steps with 150 walkers. The definitions of all the parameters used in this section are listed in Table 2. The uncertainties presented here represent only the statistical errors on the fits.

An individual power source in MOSFiT, such as a magnetar or radioactive decay, can only reproduce a single peaked light curve. Therefore, we first investigate the origin of the first peak and include only the data up to MJD = 58853 (Phase = 53 days), before the emergence of the second peak. We explore the origin of the second peak in §5.3.

5.1. Radioactive Decay

Motivated by the SN Ic spectrum of SN 2019stc, we first investigate a light curve model with heating from nickel-cobalt radioactive decay (Arnett 1982) where the

Table 3. Best-fit Parameters for the Radioactive Decay Model

Parameter	Prior	Posterior	Units
M_{ej}	[0.1, 100]	$10.3^{+1.9}_{-1.6}$	M_{\odot}
f_{Ni}	[0.0, 1]	$0.31^{+0.06}_{-0.05}$	
M_{Ni}^{\dagger}		3.2 ± 0.2	M_{\odot}
V_{ej}	7800 ± 1900	8000^{+560}_{-540}	km s^{-1}
E_k^{\dagger}		$3.9^{+1.3}_{-1.0}$	10^{51} erg
t_{exp}	[0, 50]	7.3 ± 0.7	days
T_{min}	[3000, 10^5]	3900^{+620}_{-600}	K
$\log(n_{H,\text{host}})$	[16, 23]	18.4 ± 1.6	cm^{-2}
$A_{V,\text{host}}^{\dagger}$		< 0.05	mag
$\log(\kappa_{\gamma})$	[-2, 2]	$-1.96^{+0.05}_{-0.03}$	$\text{cm}^2 \text{g}^{-1}$
$\log \sigma$	[-3, 2]	-0.77 ± 0.06	

NOTE—Best model parameters, prior ranges, and 1σ uncertainties for the model realizations shown in Figure 7. See Table 2 for parameter definitions.

[†]These parameters are calculated using the posterior distribution samples of the fitted parameters.

input luminosity is given by:

$$L_{\gamma} = M_{\text{Ni}} \left[\epsilon_{\text{Ni}} e^{-t/\tau_{\text{Ni}}} + \epsilon_0 e^{-t/\tau_{\text{Co}}} \right]. \quad (1)$$

Here t is rest-frame time; M_{Ni} is the initial mass of ^{56}Ni ; $\tau_{\text{Ni}} = 8.8$ days and $\tau_{\text{Co}} = 111.3$ days are the half-lives of ^{56}Ni and ^{56}Co , respectively (Nadyozhin 1994); $\epsilon_{\text{Ni}} = 6.45 \times 10^{43} \text{ erg s}^{-1} M_{\odot}^{-1}$ is the heating rate for ^{56}Ni ; and $\epsilon_0 = 1.45 \times 10^{43} \text{ erg s}^{-1} M_{\odot}^{-1}$ is the effective heating rate for ^{56}Co , which is a function of τ_{Ni} and τ_{Co} . We assume an opacity of $\kappa = 0.07$, determined to be a suitable value for SNe Ic (Taddia et al. 2018).

We show the best-fit realizations of this model in Figure 7 and list the best-fit parameters and associated uncertainties in Table 3. We find that the model provides a good fit to the g - and r -band light curves, but systematically over-predicts the i -band data due to a mismatch between the model and data photospheric temperatures.

As expected from the high luminosity and broad light curve, we find large values of $M_{\text{Ni}} \approx 3.2 M_{\odot}$ and $M_{\text{ej}} \approx 10.3 M_{\odot}$, leading to a high nickel fraction of $f_{\text{Ni}} \approx 0.31$. The nickel mass is substantially higher than the typical range for SNe Ic and Ic-BL of $\approx 0.05 - 0.6 M_{\odot}$ (Drout et al. 2011; Taddia et al. 2019b). In Figure 8 we compare the results for SN 2019stc to the SNe Ic sample from Barbarino et al. (2020) and the Ic-BL

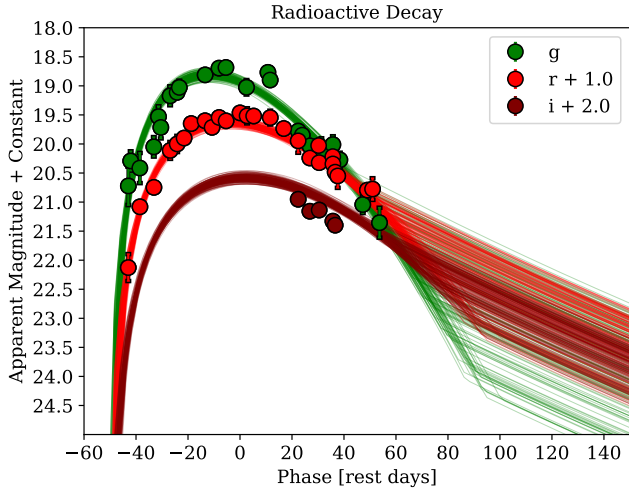


Figure 7. First peak of the light curve of SN 2019stc with the best fit MOSFiT radioactive decay model described in §5.1. Corrected for Galactic extinction.

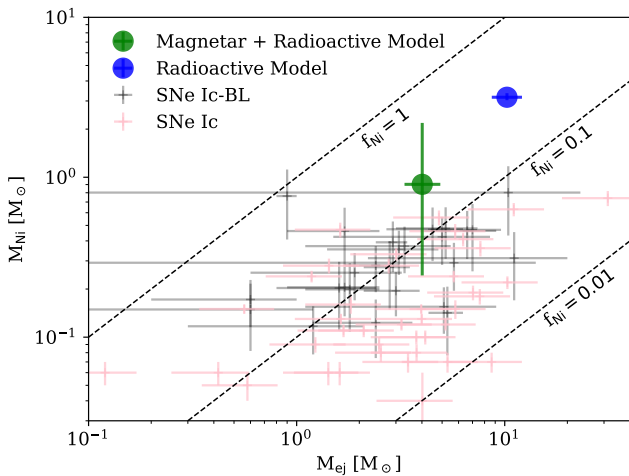


Figure 8. The ^{56}Ni mass versus ejecta mass inferred from the radioactive decay (blue) and the magnetar plus radioactive decay (green) models of SN 2019stc. Also shown for comparison are SNe Ic-BL (grey; Taddia et al. 2019b) and SNe Ic (pink; Barbarino et al. 2020) populations. Representative nickel fractions of 0.01, 0.1, and 1 are shown with dashed lines. The inferred values of M_{ej} and M_{Ni} for the radioactive decay model of SN 2019stc are well outside of the distribution for the SN Ic and Ic-BL population, while the values from the magnetar plus radioactive decay models are consistent with the SN Ic and Ic-BL population.

sample from Taddia et al. (2019b)⁵. We see that the nickel fraction found for SN 2019stc is much higher than

⁵ We exclude iPTF15eov, which is most likely a SLSN as opposed to a SN Ic-BL.

Table 4. Best-fit Parameters for the Magnetar Engine + Radioactive Decay Model

Parameter	Prior	Best-fit	Units
M_{ej}	[0.1, 100]	$4.0_{-0.7}^{+0.9}$	M_{\odot}
f_{Ni}	[0.0, 1]	$0.2_{-0.2}^{+0.3}$	
M_{Ni}^{\dagger}		$0.9_{-0.7}^{+1.3}$	M_{\odot}
M_{NS}	[1.0, 2.2]	1.7 ± 0.4	M_{\odot}
P_{spin}	[0.7, 20]	$7.2_{-1.8}^{+2.7}$	ms
θ_{PB}	[0.0, $\pi/2$]	0.9 ± 0.4	rad
B_{\perp}	$\log([0.01, 10])$	$0.9_{-0.5}^{+1.0}$	10^{14} G
V_{ej}	7800 ± 1900	6970_{-470}^{+490}	km s^{-1}
E_k^{\dagger}		$1.2_{-0.3}^{+0.4}$	10^{51} erg
t_{exp}	[0, 50]	9.9 ± 1.5	days
T_{min}	[3000, 10^5]	4100_{-760}^{+780}	K
$\log(n_{H,\text{host}})$	[16, 23]	18.6 ± 1.7	cm^{-2}
$A_{V,\text{host}}^{\dagger}$		< 0.09	mag
κ	[0.05, 0.2]	$0.18_{-0.03}^{+0.02}$	
$\log(\kappa_{\gamma})$	[-2, 2]	-1.9 ± 0.1	$\text{cm}^2 \text{g}^{-1}$
$\log \sigma$	[-3, 2]	-0.84 ± 0.06	

NOTE—Best model parameters, prior ranges, and 1σ uncertainties for the model realizations shown in Figure 9. See Table 2 for parameter definitions.

[†] These parameters are calculated using the posterior distribution samples of the fitted parameters.

typical SNe Ic, especially in the high ejecta mass regime (Figure 8). We therefore conclude that while SN 2019stc most closely resembles SNe Ic in terms of its spectra, it is unlikely to be powered exclusively by radioactive decay.

5.2. Magnetar Engine + Radioactive Decay

We next explore a model with energy input from both radioactive decay (motivated by the spectral match to a SN Ic) and a magnetar central engine (motivated by the broad and luminous first peak). The MOSFiT setup for the magnetar model (Kasen & Bildsten 2010; Woosley 2010) is described in detail in Nicholl et al. (2017b). We show the best-fit realizations of this model in Figure 9, and list the best-fit parameters and associated uncertainties in Table 4. We find an ejecta mass of $M_{\text{ej}} \approx 4 M_{\odot}$ and a nickel fraction that is consistent with 0 but extends to the typical values for SNe Ic (Figure 8). The best fit parameters of the magnetar engine are $P_{\text{spin}} \approx 7.2$ ms and $B_{\perp} \approx 1 \times 10^{14}$ G. In Figure 10 we break down the model into its two components and find that the magnetar engine dominates the energy input, accounting for $89 \pm 8\%$, while the radioactive decay component contributes only $11 \pm 4\%$ of the total energy.

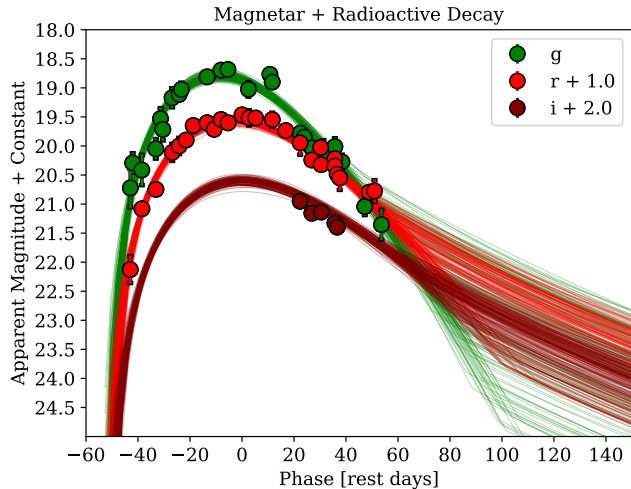


Figure 9. First peak of the light curve of SN 2019stc with the best fit MOSFiT magnetar engine plus radioactive decay model described in §5.2. Corrected for Galactic extinction.

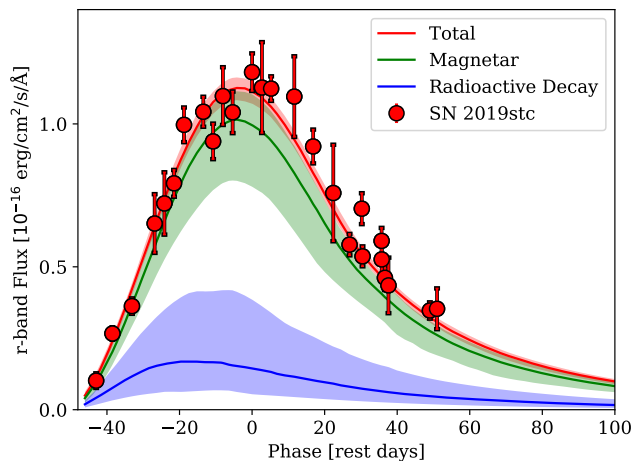


Figure 10. Best fit model realizations (lines) and their 1σ confidence intervals (shaded regions) for the magnetar engine plus radioactive decay model (red). We decompose the contribution from the magnetar engine (green) and radioactive decay (blue) components. We find that the magnetar engine clearly dominates the energy input.

In Figure 11 we compare the magnetar engine parameters of SN 2019stc to the SLSNe samples from Nicholl et al. (2017b), Villar et al. (2018), and Blanchard et al. (2020), which were also modeled with MOSFiT. We find that the spin period for SN 2019stc is in the slow end of the distribution for SLSNe, as expected from its moderate peak luminosity compared to the bulk of the SLSN sample. Still, the magnetar engine parameters for SN 2019stc are not outside of the distribution for SLSNe.

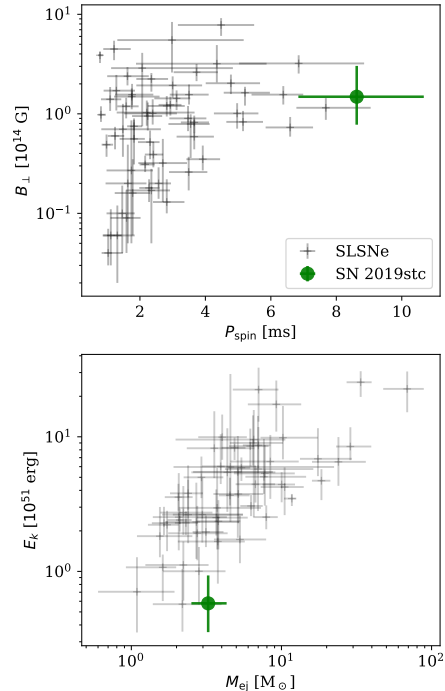


Figure 11. The best fit magnetar engine parameters for SN 2019stc (green) compared to those of SLSNe (black; Nicholl et al. 2017b; Villar et al. 2018; Blanchard et al. 2020). As expected from the moderate luminosity of SN 2019stc, the magnetar has a slower initial spin than most SLSNe, but the parameters do overlap the known distribution.

We therefore conclude that the first peak of SN 2019stc is best explained with a predominant magnetar engine contribution, but with a non-zero contribution from radioactive heating. This combination explains the appearance of both the first peak of the light curve and the spectra.

5.3. Second Light Curve Peak: Circumstellar Interaction

We have so far excluded the second peak from our model fits since a single power source (or even a combined magnetar plus radioactive decay power source) cannot naturally produce a double-peaked light curve structure. To investigate the origin of the second peak we subtract the best fit magnetar plus radioactive heating model from the bolometric light curve of SN 2019stc; see Figure 12. We find that the residuals are well modeled as a Gaussian profile, with a center phase of 79.0 ± 0.4 days, a width of $\text{FWHM} = 30.9 \pm 1.2$ days, and a total integrated radiated energy of $(8.5 \pm 0.3) \times 10^{49}$ erg. We stress that the energy radiated in the second peak alone is larger than for most normal SNe Ic (Prentice et al. 2016).

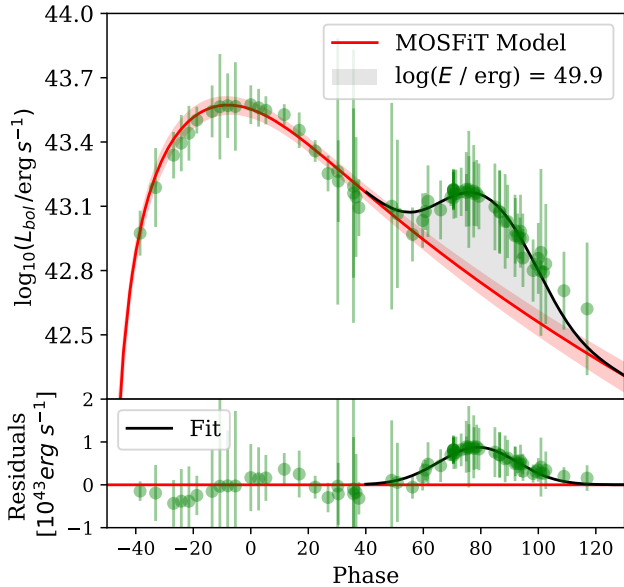


Figure 12. *Top:* Bolometric light curve of SN 2019stc (green points) along with the best-fit magnetar engine plus radioactive decay model realizations (red band). The shaded grey region indicates the integrated energy in the second peak, $E_{\text{rad}} \approx 8.5 \times 10^{49}$ erg. *Bottom:* Residuals of the bolometric light curve relative to the first peak model, demonstrating that the second peak is well modeled by a Gaussian profile (black).

We find that the decline rate past the second peak is ~ 0.04 mag day $^{-1}$, much more rapid than the decline rate for Co decay (~ 0.01 mag day $^{-1}$). Therefore, the second peak is unlikely to be caused by radioactive decay. Moreover, to produce such a pronounced excess of radiated energy at late time, with a peak luminosity of $\approx 10^{43}$ erg s $^{-1}$, would require a prohibitive mass of radioactive material ($M_{\text{Ni}} \approx 1.5 M_{\odot}$) buried deep in the ejecta so as not to produce detectable emission during the first peak. This is inconsistent with our finding that the photospheric radius is comparable from the first to the second peak.

We investigate the possibility that the second peak is powered by a magnetar engine with an unusually slow spin-down timescale (i.e., in this case the first peak would be dominated by radioactive heating, a model that we already disfavored in §5.1). However, we find that the very slow rise time of ~ 120 days required in this context is inconsistent with the fast decline time of ~ 20 days after the second peak.

Having ruled out radioactive decay and a magnetar engine, this leaves the possibility that the second peak is powered by CSM interaction. To explore this model we fit the residual bolometric light curve with a modified version of the CSM interaction model of Chatzopoulos

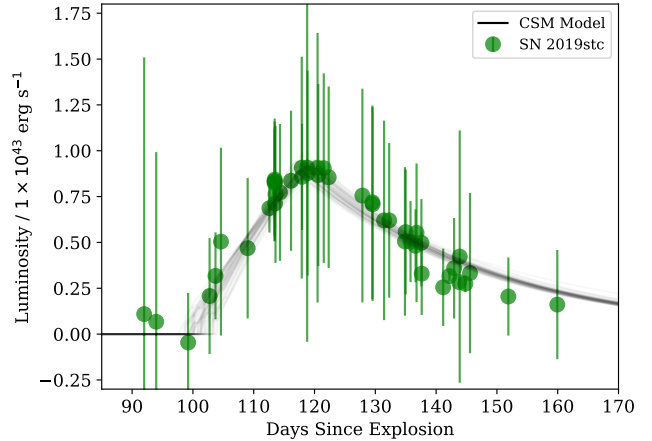


Figure 13. Residual bolometric light curve of the second peak (Figure 9), along with the best-fit realizations of a CSM interaction model (grey). We find that this model can capture the overall shape of the second peak.

et al. (2013) that allows the CSM to be a detached shell located at an arbitrary distance from the progenitor. The allowed density profiles of the ejecta range from $\rho \propto R$ to $\rho \propto R^{-2}$ and are described in Jiang et al. (2020). We use the relevant parameters of the best-fit magnetar plus radioactive decay model (§5.2) as fixed inputs: $V_{\text{ej}} = 6970$ km s $^{-1}$ and $M_{\text{ej}} = 4 M_{\odot}$. We further assume that the CSM inside the detached shell has a wind-like density profile of $\rho \propto R^{-2}$. The remaining free parameters of the model are the CSM mass (M_{CSM}), the opacity (κ), the inner radius of the CSM shell (R_0), and the density at R_0 (ρ_0). In Figure 13 we show the best fit realizations of this model, which give $M_{\text{CSM}} = 0.7 \pm 0.2 M_{\odot}$, $\kappa = 0.23 \pm 0.05$, $R_0 = 400 \pm 11$ AU, and $\log(\rho_0/\text{g cm}^{-3}) = -13.97 \pm 0.05$.

We stress that given the normal SN Ic spectrum during the second peak, the CSM shell must be hydrogen and helium poor. With a radius of about 400 AU, and assuming a CSM velocity of $\sim 10^3$ km s $^{-1}$, expected for a compact stripped star, we find that the shell must have been ejected about 2 years before the SN explosion. If powered by CSM interaction, the lack of narrow emission features during the second peak might be the product of either the composition of the ejecta or an aspherical CSM. (Soumagnac et al. 2020) showed that an increasing photospheric radius is observed in SNe with aspherical CSMs, and that asphericity is more common in brighter SNe; both features we observe in SN 2019stc.

Even though we disfavor the radioactive heating model, for completeness we perform the same CSM modeling using the parameters from this model. The relevant values from the radioactive decay model presented in §5.1 are: $V_{\text{ej}} = 8000$ km s $^{-1}$, $M_{\text{ej}} = 10.3$

M_{\odot} , and $\kappa = 0.07$. For this model we find a larger CSM mass, $M_{\text{CSM}} = 3.4 \pm 0.1 M_{\odot}$, a larger inner radius, $R_0 = 490 \pm 5$ AU, and a lower density of $\log(\rho_0/g \text{ cm}^{-3}) = -13.34 \pm 0.02$.

6. HOST GALAXY

Archival PS1/3 π images reveal a galaxy near the location of SN 2019stc. Using our deep late-time images (which contain no detectable SN light contribution), we measure a half-light radius of $0.68 \pm 0.15''$ for this galaxy and a projected spatial offset of $0.74 \pm 0.05''$ (Figure 1). We follow the method described in Bloom et al. (2002) and Berger (2010) to determine that this galaxy has a probability of chance coincidence of $P_{\text{cc}} = 0.004$. In conjunction with the fact that the SN features agree with the host redshift, this means that this galaxy is clearly associated with SN 2019stc. We measure a redshift of $z = 0.117 \pm 0.001$ by measuring the position of the narrow host galaxy emission lines H α , H β , [O II] $\lambda\lambda 3726, 3729$, and [O III] $\lambda\lambda 4959, 5007$. The relevant host galaxy parameters are listed in Table 5.

We measure a flux ratio of $L_{\text{H}\alpha}/L_{\text{H}\beta} = 2.3 \pm 0.8$ through a weighted average of all SN spectra. This value is consistent with case B recombination ($L_{\text{H}\alpha}/L_{\text{H}\beta} = 2.86$) indicating no significant host galaxy extinction. This agrees with the results of our MOSFIT modeling (Tables 3 and 4). From the flux of the H α line we estimate the star formation rate to be $\text{SFR} = (0.11 \pm 0.01) M_{\odot} \text{ yr}^{-1}$ using the relation of Kennicutt (1998).

We infer the metallicity using the R_{23} method (Kobulnicky et al. 1999), which is double-valued, but the lack of detectable [N II] emission points to the lower branch solution. This gives a value of $12 + \log(\text{O}/\text{H}) = 8.1 \pm 0.1$, or $Z = 0.26 \pm 0.07 Z_{\odot}$ (Asplund et al. 2009). This is an unusually low metallicity for SN Ic hosts, higher than only 7% ($N = 2$) of the normal SNe Ic from the study of Modjaz et al. (2020) when comparing to their KD02 calibration (Kewley & Dopita 2002). Instead, the low metallicity is more typical of SLSN hosts, which cluster around $12 + \log(\text{O}/\text{H}) = 8.4 \pm 0.3$ (Lunnan et al. 2014). Further supporting the magnetar engine interpretation for SN 2019stc.

7. DISCUSSION AND CONCLUSIONS

We presented optical photometry and spectroscopy of SN 2019stc, which we determine to be a Type Ic SN at $z = 0.117$ with a luminous, broad, and peculiar double-peaked light curve. The two light curve peaks are separated by about 80 days and are both more prominent and further apart than in other stripped SNe with distinct peaks. From analytic modeling we conclude that SN 2019stc is powered by three distinct power sources:

Table 5. Host Galaxy Properties

	Value	Units
P_{cc}	0.004	
z	0.117 ± 0.001	
D_L	562 ± 5	Mpc
D	0.74 ± 0.05	arcsec
D	2.0 ± 0.1	kpc
r_{50}	1.85 ± 0.55	kpc
g	22.29 ± 0.09	mag
r	22.09 ± 0.05	mag
i	21.99 ± 0.05	mag
z	22.04 ± 0.10	mag
y	21.90 ± 0.21	mag
M_g	-16.67 ± 0.09	mag
M_r	-16.77 ± 0.05	mag
M_i	-16.82 ± 0.05	mag
M_z	-16.72 ± 0.10	mag
M_y	-16.84 ± 0.21	mag
L_g	0.0348 ± 0.0030	L_*
L_r	0.0128 ± 0.0007	L_*
L_i	0.0109 ± 0.0006	L_*
L_z	0.0064 ± 0.0006	L_*
$L_{\text{H}\alpha}$	14.3 ± 1.3	$10^{39} \text{ erg s}^{-1}$
$L_{\text{H}\beta}$	6.1 ± 1.1	$10^{39} \text{ erg s}^{-1}$
$L_{[\text{OII}]_{3726,3729}}$	13.3 ± 3.3	$10^{39} \text{ erg s}^{-1}$
$L_{[\text{OIII}]_{4959}}$	7.6 ± 1.8	$10^{39} \text{ erg s}^{-1}$
$L_{[\text{OIII}]_{5007}}$	21.6 ± 5.3	$10^{39} \text{ erg s}^{-1}$
$12 + \log(\text{O}/\text{H})$	8.1 ± 0.1	
Z_{23}	0.26 ± 0.07	Z_{\odot}
SFR	0.11 ± 0.01	$M_{\odot} \text{ yr}^{-1}$

NOTE—List of measured and derived properties of the host galaxy of SN 2019stc. P_{cc} is the probability of chance coincidence, z is the redshift, D_L is the luminosity distance, D is the offset of SN 2019stc from the center of its host galaxy, r_{50} is the half-light Petrosian radius in the r -band, $grizy$ are host magnitudes before correcting for Galactic extinction, M_{grizy} are the host absolute magnitudes after correcting for Galactic extinction and including a cosmological K-correction, L_{griz} are the host luminosities relative to L_* in each band (Montero-Dorta & Prada 2009), L_n are the integrated luminosities of several key emission lines (H α , H β , [O II], [O III]), $12 + \log(\text{O}/\text{H})$, Z_{23} are values for the host metallicity inferred from the R23 formalism, and SFR is the star formation rate.

a magnetar central engine, radioactive decay, and CSM interaction, with the first two powering the first peak, and the latter producing the second peak. Another example of a SN suggested to be powered by radioactive decay, a magnetar central engine, and CSM interaction was iPTF13ehe (Wang et al. 2016).

Compared to the overall population of SLSNe, the magnetar engine in SN 2019stc is much less powerful ($P_{\text{spin}} \sim 7$ ms and $B_{\perp} \sim 10^{14}$ G), and this is expected to lead to a lower temperature that would not generate the distinctively blue spectrum of SLSNe near peak. This, along with a relatively higher contribution from radioactive heating compared to the more luminous SLSNe, can explain the SN Ic spectrum of SN 2019stc near peak. Indeed, the spectrum of SN 2019stc near peak resembles SLSN spectra well after peak, once the engine power has declined and the ejecta have significantly cooled (e.g., SN 2015bn: Nicholl et al. 2019, SN 2010gx: Pastorello et al. 2010). Thus, the spectral appearance and first peak light curve characteristics of SN 2019stc appear to be consistent within our magnetar engine plus radioactive heating model.

We find that the prominent second peak of SN 2019stc is instead powered by interaction with $\sim 0.7 M_{\odot}$ of hydrogen-free CSM located about 400 AU from the progenitor (corresponding to ejection about 2 years pre-explosion). Although only a handful of SLSNe show possible evidence for late-time hydrogen emission (Yan et al. 2020b), the light curve “bumps” in other SLSNe have been suggested to result from CSM interaction (e.g., Nicholl et al. 2016a; Inserra et al. 2017; Blanchard et al. 2018; Lunnan et al. 2020; Jin et al. 2021). These bumps, however, are significantly less pronounced than in SN 2019stc, and the inferred CSM masses required to produce them are $\lesssim 0.05 M_{\odot}$, more than an order of magnitude lower than in SN 2019stc.

Combining the ejecta mass of $\approx 4 M_{\odot}$, CSM shell mass of $\approx 0.7 M_{\odot}$, and remnant neutron star mass of $\approx 1.7 M_{\odot}$, we infer a total pre-explosion progenitor CO core mass of $\approx 6.5 M_{\odot}$. The ejecta mass for SN 2019stc is within the range of typical ejecta masses of SNe Ic, which center around $M_{\text{ej}} = 4.5 \pm 0.8 M_{\odot}$ (Barbarino et al. 2020), but the CO core mass also overlaps with the progenitor mass distribution for SLSNe, which have mean masses of $6.4_{-2.8}^{+8.1} M_{\odot}$ (Blanchard et al. 2020).

The large CSM density and proximity to the progenitor indicate the $0.7 M_{\odot}$ were ejected within a span of ~ 0.1 years about 2 years before explosion. SNe

with high mass-loss events have been observed previously (e.g., SN 2014C Milisavljevic et al. 2015; SN 2009ip Margutti et al. 2014), but the CSM in these events was hydrogen-rich. Large mass-loss events are also a key feature of pulsational pair-instability SNe (PPISNe; Woosley et al. 2007). We note however that the progenitor mass estimate of SN 2019stc is well below the required CO core mass of $\gtrsim 25 M_{\odot}$ required to produce a PPISNe (Woosley et al. 2007).

In conclusion, SN 2019stc is a peculiar stripped SN that occupies the mostly unexplored regime between SLSNe and SNe Ic, and shares properties with both. Its peak luminosity is on the low end for SLSNe, but high for SNe Ic and Ic-BL. Its first-peak light curve is unusual for SNe Ic but can be accommodated with the same models that explain SLSNe. Its host environment has a low metallicity, much like those of SLSNe and its pre-explosion progenitor mass is consistent with those of both SNe Ic and SLSNe.

We thank Y. Beletsky for carrying out some of the Magellan observations. The Berger Time-Domain Group at Harvard is supported by NSF and NASA grants. This work is supported in part by the National Science Foundation under Cooperative Agreement PHY-2019786 (The NSF AI Institute for Artificial Intelligence and Fundamental Interactions, <http://iaifi.org/>). S. Gomez is partly supported by an NSF Graduate Research Fellowship. This paper includes data gathered with the 6.5 meter Magellan Telescopes located at Las Campanas Observatory, Chile. Observations reported here were obtained at the MMT Observatory, a joint facility of the University of Arizona and the Smithsonian Institution. This research has made use of NASA’s Astrophysics Data System. This research has made use of the SIMBAD database, operated at CDS, Strasbourg, France.

Software: Astropy(Astropy Collaboration et al. 2018), MOSFiT(Guillochon et al. 2018), FLEET(Gomez et al. 2020b), PyRAF(Science Software Branch at STScI 2012), SAOImage DS9(Smithsonian Astrophysical Observatory 2000), emcee(Foreman-Mackey et al. 2013), corner(Foreman-Mackey 2016), HOTPANTS(Becker 2015), Superbol(Nicholl 2018), Matplotlib(Hunter 2007), SciPy(van der Walt et al. 2011), NumPy(Oliphant 2007), extinction(Barbary 2016), PYPHOT(<https://github.com/mfouesneau/pyphot>).

REFERENCES

- Anderson, J. P., Pessi, P. J., Dessart, L., et al. 2018, *A&A*, **620**, A67
- Angus, C. R., Smith, M., Sullivan, M., et al. 2019, *MNRAS*, **487**, 2215

- Arnett, W. D. 1982, *ApJ*, **253**, 785
- Asplund, M., Grevesse, N., Sauval, A. J., & Scott, P. 2009, *ARA&A*, **47**, 481
- Astropy Collaboration, Price-Whelan, A. M., Sipőcz, B. M., et al. 2018, *AJ*, **156**, 123
- Barbarino, C., Sollerman, J., Taddia, F., et al. 2020, arXiv e-prints, [arXiv:2010.08392](https://arxiv.org/abs/2010.08392)
- Barbary, K. 2016, extinction, v0.3.0, Zenodo, doi:[10.5281/zenodo.804967](https://doi.org/10.5281/zenodo.804967)
- Becker, A. 2015, HOTPANTS: High Order Transform of PSF ANd Template Subtraction, [ascl:1504.004](https://arxiv.org/abs/1504.004)
- Bellm, E. C., Kulkarni, S. R., Graham, M. J., et al. 2019, *PASP*, **131**, 018002
- Berger, E. 2010, *ApJ*, **722**, 1946
- Blanchard, P. K., Berger, E., Nicholl, M., & Villar, V. A. 2020, *ApJ*, **897**, 114
- Blanchard, P. K., Nicholl, M., Berger, E., et al. 2019, *ApJ*, **872**, 90
- Blanchard, P. K., Nicholl, M., Berger, E., et al. 2018, *ApJ*, **865**, 9
- Bloom, J. S., Kulkarni, S. R., & Djorgovski, S. G. 2002, *AJ*, **123**, 1111
- Cardelli, J. A., Clayton, G. C., & Mathis, J. S. 1989, in *Interstellar Dust*, ed. L. J. Allamandola & A. G. G. M. Tielens, Vol. 135, 5–10
- Chambers, K., & Pan-STARRS Team. 2018, in *American Astronomical Society Meeting Abstracts*, Vol. 231, *American Astronomical Society Meeting Abstracts #231*, 102.01
- Chatzopoulos, E., Wheeler, J. C., Vinko, J., Horvath, Z. L., & Nagy, A. 2013, *ApJ*, **773**, 76
- Chomiuk, L., Chornock, R., Soderberg, A. M., et al. 2011, *ApJ*, **743**, 114
- Dressler, A., Bigelow, B., Hare, T., et al. 2011, *PASP*, **123**, 288
- Drout, M. R., Soderberg, A. M., Gal-Yam, A., et al. 2011, *ApJ*, **741**, 97
- Fabricant, D., Fata, R., Epps, H., et al. 2019, *PASP*, **131**, 075004
- Fabricant, D. G., Epps, H. W., Brown, W. L., Fata, R. G., & Mueller, M. 2003, in *Society of Photo-Optical Instrumentation Engineers (SPIE) Conference Series*, Vol. 4841, *Instrument Design and Performance for Optical/Infrared Ground-based Telescopes*, ed. M. Iye & A. F. M. Moorwood, 1134–1144
- Filippenko, A. V. 1997, *ARA&A*, **35**, 309
- Foreman-Mackey, D. 2016, *The Journal of Open Source Software*, **1**
- Foreman-Mackey, D., Hogg, D. W., Lang, D., & Goodman, J. 2013, *PASP*, **125**, 306
- Fremling, C., Sollerman, J., Kasliwal, M. M., et al. 2018, *A&A*, **618**, A37
- Gal-Yam, A. 2012, *Science*, **337**, 927
- Gal-Yam, A. 2019, *ARA&A*, **57**, 305
- Galama, T. J., Vreeswijk, P. M., van Paradijs, J., et al. 1998, *Nature*, **395**, 670
- Gelman, A., & Rubin, D. B. 1992, *Statistical Science*, **7**, 457
- Gomez, S., Berger, E., Blanchard, P. K., et al. 2020a, *ApJ*, **904**, 74
- Gomez, S., Berger, E., Blanchard, P. K., et al. 2020b, FLEET Finding Luminous and Exotic Extragalactic Transients, 1.0.0, Zenodo, doi:[10.5281/zenodo.4013965](https://doi.org/10.5281/zenodo.4013965)
- Gomez, S., Berger, E., Nicholl, M., et al. 2019, *ApJ*, **881**, 87
- Greiner, J., Mazzali, P. A., Kann, D. A., et al. 2015, *Nature*, **523**, 189
- Guillochon, J., Nicholl, M., Villar, V. A., et al. 2018, *ApJS*, **236**, 6
- Guillochon, J., Parrent, J., Kelley, L. Z., & Margutti, R. 2017, *ApJ*, **835**, 64
- Hinshaw, G., Larson, D., Komatsu, E., et al. 2013, *ApJS*, **208**, 19
- Ho, A. Y. Q., Goldstein, D. A., Schulze, S., et al. 2019, *ApJ*, **887**, 169
- Howell, D. A., Kasen, D., Lidman, C., et al. 2013, *ApJ*, **779**, 98
- Hunter, J. D. 2007, *Computing in Science and Engineering*, **9**, 90
- Inserra, C., Nicholl, M., Chen, T. W., et al. 2017, *MNRAS*, **468**, 4642
- Jiang, B., Jiang, S., & Ashley Villar, V. 2020, *Research Notes of the American Astronomical Society*, **4**, 16
- Jin, H., Yoon, S.-C., & Blinnikov, S. 2021, arXiv e-prints, [arXiv:2101.11171](https://arxiv.org/abs/2101.11171)
- Kasen, D., & Bildsten, L. 2010, *ApJ*, **717**, 245
- Kennicutt, Robert C., J. 1998, *ARA&A*, **36**, 189
- Kewley, L. J., & Dopita, M. A. 2002, *ApJS*, **142**, 35
- Kobulnicky, H. A., Kennicutt, Robert C., J., & Pizagno, J. L. 1999, *ApJ*, **514**, 544
- Lunnan, R., Chornock, R., Berger, E., et al. 2013, *ApJ*, **771**, 97
- Lunnan, R., Chornock, R., Berger, E., et al. 2014, *ApJ*, **787**, 138
- Lunnan, R., Yan, L., Perley, D. A., et al. 2020, *ApJ*, **901**, 61
- Lyman, J. D., Bersier, D., James, P. A., et al. 2016, *MNRAS*, **457**, 328
- Margutti, R., Milisavljevic, D., Soderberg, A. M., et al. 2014, *ApJ*, **780**, 21
- Mazzali, P. A., Sauer, D. N., Pian, E., et al. 2017, *MNRAS*, **469**, 2498

- Milisavljevic, D., Margutti, R., Kamble, A., et al. 2015, *ApJ*, 815, 120
- Modjaz, M., Blondin, S., Kirshner, R. P., et al. 2014, *AJ*, 147, 99
- Modjaz, M., Bianco, F. B., Siwek, M., et al. 2020, *ApJ*, 892, 153
- Montero-Dorta, A. D., & Prada, F. 2009, *MNRAS*, 399, 1106
- Nadyozhin, D. K. 1994, *ApJS*, 92, 527
- Nicholl, M. 2018, *Research Notes of the American Astronomical Society*, 2, 230
- Nicholl, M., Berger, E., Blanchard, P. K., Gomez, S., & Chornock, R. 2019, *ApJ*, 871, 102
- Nicholl, M., Berger, E., Margutti, R., et al. 2017a, *ApJL*, 845, L8
- Nicholl, M., Guillochon, J., & Berger, E. 2017b, *ApJ*, 850, 55
- Nicholl, M., Berger, E., Smartt, S. J., et al. 2016a, *ApJ*, 826, 39
- Nicholl, M., Berger, E., Margutti, R., et al. 2016b, *ApJ*, 828, L18
- Nicholl, M., Blanchard, P. K., Berger, E., et al. 2018, *ApJ*, 866, L24
- Oliphant, T. E. 2007, *CSE*, 9, 10
- Pastorello, A., Smartt, S. J., Botticella, M. T., et al. 2010, *ApJL*, 724, L16
- Patat, F., Cappellaro, E., Danziger, J., et al. 2001, *ApJ*, 555, 900
- Prentice, S. J., Mazzali, P. A., Pian, E., et al. 2016, *MNRAS*, 458, 2973
- Prentice, S. J., Ashall, C., James, P. A., et al. 2019, *MNRAS*, 485, 1559
- Quimby, R. M., Kulkarni, S. R., Kasliwal, M. M., et al. 2011, *Nature*, 474, 487
- Quimby, R. M., De Cia, A., Gal-Yam, A., et al. 2018, *ApJ*, 855, 2
- Roy, R., Sollerman, J., Silverman, J. M., et al. 2016, *A&A*, 596, A67
- Schlafly, E. F., & Finkbeiner, D. P. 2011, *ApJ*, 737, 103
- Schmidt, G. D., Weymann, R. J., & Foltz, C. B. 1989, *PASP*, 101, 713
- Science Software Branch at STScI. 2012, PyRAF: Python alternative for IRAF, Astrophysics Source Code Library, [ascl:1207.011](https://www.ascl.net/1207.011)
- Smithsonian Astrophysical Observatory. 2000, SAOImage DS9: A utility for displaying astronomical images in the X11 window environment, [ascl:0003.002](https://www.ascl.net/0003.002)
- Soumagnac, M. T., Ofek, E. O., Liang, J., et al. 2020, *ApJ*, 899, 51
- Stevenson, K. B., Bean, J. L., Seifahrt, A., et al. 2016, *ApJ*, 817, 141
- Taddia, F., Sollerman, J., Fremling, C., et al. 2019a, *A&A*, 621, A64
- Taddia, F., Stritzinger, M. D., Bersten, M., et al. 2018, *A&A*, 609, A136
- Taddia, F., Sollerman, J., Fremling, C., et al. 2019b, *A&A*, 621, A71
- Taubenberger, S., Pastorello, A., Mazzali, P. A., et al. 2006, *MNRAS*, 371, 1459
- van der Walt, S., Colbert, S. C., & Varoquaux, G. 2011, *CSE*, 13, 22
- Villar, V. A., Nicholl, M., & Berger, E. 2018, *ApJ*, 869, 166
- Wang, S. Q., Liu, L. D., Dai, Z. G., Wang, L. J., & Wu, X. F. 2016, *ApJ*, 828, 87
- Woosley, S. E. 2010, *ApJ*, 719, L204
- Woosley, S. E., Blinnikov, S., & Heger, A. 2007, *Nature*, 450, 390
- Yan, L., Perley, D., Schulze, S., et al. 2020a, Transient Name Server Classification Report, [2020-1737](https://www.ascl.net/2020-1737), 1
- Yan, L., Lunnan, R., Perley, D. A., et al. 2017, *ApJ*, 848, 6
- Yan, L., Perley, D. A., Schulze, S., et al. 2020b, *ApJL*, 902, L8
- Yaron, O., & Gal-Yam, A. 2012, *PASP*, 124, 668